Available online at www.sciencedirect.com

jmr&t Journal of Materials Research and Technology

journal homepage: www.elsevier.com/locate/jmrt

Original Article

Thermal process and material flow during dissimilar double-sided friction stir spot welding of AZ31/ZK60 magnesium alloys

W.C. Ke [a], J.P. Oliveira [b], S.S. Ao [c], F.B. Teshome [a], L. Chen [a], B. Peng [a], Z. Zeng [a,*]

[a] School of Mechanical and Electrical Engineering, University of Electronic Science and Technology of China, Sichuan, 611731, China

[b] UNIDEMI, Department of Mechanical and Industrial Engineering, NOVA School of Science and Technology, NOVA University Lisbon, 2829-516, Caparica, Portugal

[c] School of Materials Science and Engineering, Tianjin University, Tianjin, 300072, China

ARTICLE INFO

Article history:
Received 5 November 2021
Accepted 18 January 2022
Available online 23 January 2022

Keywords:
Friction stir spot welding
Dissimilar welding
Material flow
Computational fluid dynamics (CFD)
Magnesium alloy

ABSTRACT

A computational fluid dynamics (CFD) model for double-sided friction stir spot welding (FSSW) between AZ31 and ZK60 magnesium alloys using adjustable pins is proposed in this paper. Multiple phase flow theories are combined to track the metal interface and phase distribution using FLUENT software. The heat transfer and material flow for the 5 stages of the friction stir welding process, including the pre-heating, plunging, welding, rising and post-heating stages, are presented. For further evaluation, the calculated flow and thermal responses are compared with experimental data, which overall showed good agreement. The material between the upper and lower pins is softened after the pre-heating process and is then driven by the plunging pin to form a keyhole below the upper tool and a bulge region in the bottom of the plates. The welding interface between the pins is bowl-shaped after plunging, and grows uneven during the welding stage due to the extensive plastic material flow. The keyhole is then fully eliminated after the rising of the pins. After welding, the region between the tools is heated to a maximum temperature of 670 K and the welding interface slightly fluctuates and a phase mixing phenomenon occurs, suggesting that AZ31 and ZK60 plates are well joined by using the adjustable pins.

1. Introduction

As the lightest structural metal, magnesium alloys are expected to replace both aluminum and steel components in the automotive and aerospace industries [1,2], thereby reducing vehicle weight, fuel requirements, and the emission of harmful greenhouse gases [3]. Due to the poor plastic formability of magnesium alloys, reliable welding processes are demanded to develop applications based on these materials

* Corresponding author.
E-mail address: zhizeng@uestc.edu.cn (Z. Zeng).

https://doi.org/10.1016/j.jmrt.2022.01.097

[4]. As a result of welding defects, such as the formation of oxide films, cracks and porosities, magnesium alloys are usually not well bonded by traditional fusion-based methods [5,6]. As a solid-state welding process, friction stir spot welding (FSSW) of magnesium alloys is effective to suppress such defects thus attracting great interest [7]. However, owing to the insertion of the pin, several problems, involving the formation of a keyhole, thickness reduction and bulge on the surface of the joints, will occur [8,9]. To eliminate the keyhole, Xu et al. [10] employed the refill friction stir spot welding (RFSSW) process to fabricate high-strength spot joints, however, internal void defects always form on the bottom edge of the stir zone. Lyu et al. [11] and Cox et al. [12] found that when a double-sided FSSW technique was applied and pinless tools were used on both sides, no keyhole would appear after welding. Currently, a flat friction stir spot welding setup using double-sided adjustable tools (Flat DSAT FSSW) was proposed [13–15], which is promising to obtain joints with good mechanical properties and sound surface appearance without keyhole and void defects.

In the conventional FSSW process, multiple phenomena occur, which include significant plastic deformation, high viscosity flow, and solid state bonding [16]. With the use of different base materials, welding parameters and tool geometries, the thermal process and material flow become complex and greatly depend on the combination of all those features [17]. In terms of the independent rotation and movement of the double-sided adjustable tools in Flat DSAT FSSW, the process becomes more complicated and so it is more complex to understand the underlying physical mechanisms occurring within the processed material. As mentioned by Wang et al. [18], the complex material behavior will affect the heat transfer and material flow, and this will dictate the microstructure evolution and resulting mechanical properties. As such, there is an urgent need for a basic understanding of the physical interactions that occur during this manufacturing process. Physics-based numerical models validated by experiments can aid in understanding the heat generation, temperature distribution and material flow during FSSW-based process.

Significant progress has been obtained in the qualitative understanding of traditional FSSW processes based on numerical methods. Mandal et al. [19] developed a 3-dimensional finite element model (FEM) with the commercial software ABAQUS to understand the thermal mechanics and tool wear during the plunging stage of the FSSW process. Garcia-Castillo et al. [20] further evaluated the stress and strain distribution under different parameters of the FSSW process through a finite element analysis (FEA). For a comprehensive analysis of the full RFSSW process, Xiong et al. [21] developed a coupled Eulerian–Lagrangian (CEL) model to predict the plastic material refilling procedure and reveal the mechanism of void formation. To date, the Flat DSAT FSSW has not been numerical studied in detail. Recently, Wang et al. [22] carried out Flat DSAT FSSW experiments to obtain dissimilar joints between AZ31 and ZK60 magnesium alloys. Although the authors have analyzed the welding interface and resulting mechanical properties, the interface evolution is not clear, and the existing numerical models can not properly reveal the physical mechanism in Flat DSAT FSSW process, such as the keyhole elimination, dissimilar material plastic flow and distribution. Computational fluid dynamics (CFD) modelling coupled with thermo-hydrodynamic analysis using commercial software FLUENT has been shown to be helpful in predicting the temperature history, material flow and distribution during dissimilar friction stir welding [23,24]. Here, the multiphase flow theory and Volume of Fluid (VOF) methods are introduced to represent the stirring, mixing and distribution of the materials during welding since the two metals are treated as different phases with high viscosities.

In this paper, a three-dimensional CFD model is proposed to study the thermal process, dissimilar material flow and interface evolution in Flat DSAT FSSW process of AZ31 and ZK60 magnesium alloys. The rotations of the double-sided shoulders and tool pins are taken into account to predict the heat generation. The welding interface between AZ31 and ZK60 magnesium plates is tracked by using VOF method with FLUENT software. The calculated predictions are then compared with experimental data. These results lay the foundations for establishing and optimizing the system of Flat DSAT FSSW process for actual applications.

2. Experimental procedure

The Flat DSAT FSSW system used in this work is schematically depicted in Fig. 1a. For the welding experiments, AZ31 and ZK60 magnesium alloy plates with dimensions of 150 mm × 50 mm × 2 mm were used. The chemical composition of the materials is presented in Table 1. Double-sided tools, comprised of shoulders and pins with radius of 12 and 6 mm, respectively, have flat surfaces to pursue a sound appearance of joints.

In the present research, the optimized process parameters as obtained in the work of Wang et al. [18,22] were adopted since these resulted in joints with sound appearance, strengthened welding interface and excellent mechanical properties. As Fig. 1b depicted, the Flat DSAT FSSW process is mainly composed of 5 stages, i.e., the pre-heating, plunging, welding, rising and post-heating stages. The tool rotates at a constant a rotational speed, 150 rpm, throughout the 5 stages, with the upper shoulder and pin rotating clockwise and the lower ones rotating counterclockwise. The process is initiated with the pre-heating stage, during which the tool contacts with the workpiece and keeps rotating for 2 s to soften the material near the tool. Then a plunging process is performed, in which the lower and upper pins move downward at a speed of 1.5 mm/s until a keyhole with a depth of 2.5 mm is formed. Next is the welding stage during which the plunged tool continues to rotate for 2 s. By keeping the keyhole depth equal to 2.5 mm, which is slightly higher than the plate thickness, the plunged and rotated pin will enlarge the bonded region to obtain sound joints [18]. Following is the rising stage. Different from the plunging stage, during the rising stage the upper pin moves upward by 2.5 mm firstly, and then the lower pin rises until the keyhole is fully eliminated. Therefore, the time of the plunging stage, Δt (1.67 ms), is half of the time of the rising stage. Finally, the tool will remain rotating for 2 s for post-heating.

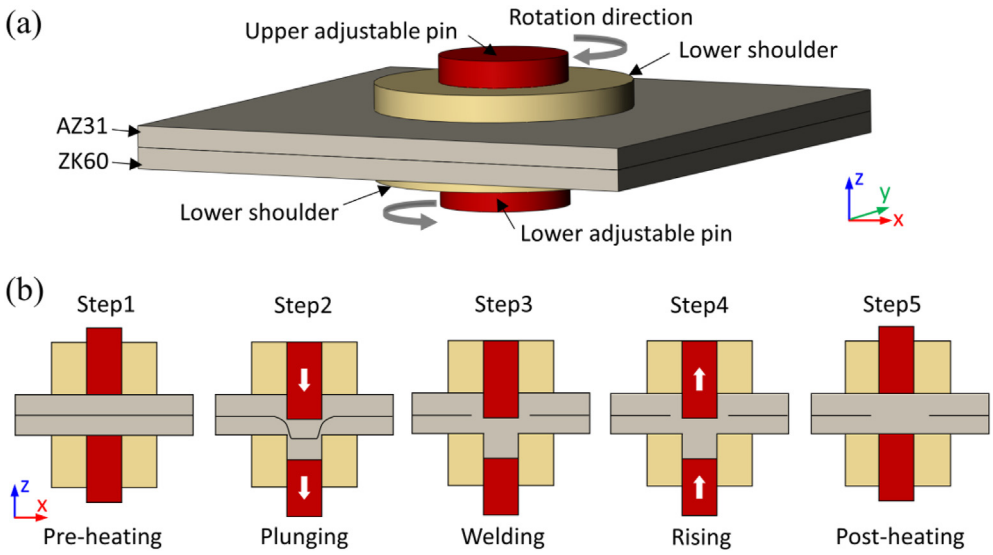

Fig. 1 – (a) Diagram of the Flat DSAT FSSW system; (b) Schematic sketch of the welding process.

3. Mathematical model

In this work, a three-dimensional mathematical model is developed to calculate the thermal process, material flow and mixing during the FSSW process by using commercial CFD software FLUENT. Several assumptions, commonly used in modelling for this type of work, were made as detailed next:

1) The metal is taken as an incompressible fluid with non-Newtonian viscosity [25].
2) The plastic material flow is laminar [25].
3) The gap between the AZ31 and ZK60 plates is ignored [24].
4) The interfacial tension between the dissimilar alloys is neglected since its effect is inapparent compared with that of the flow stress of materials with high viscosity during friction stir welding [24].

3.1. Governing equations

The governing equations of mass, momentum, and energy can be described as previously detained by Sun et al. [26]:

$$\frac{\partial \rho}{\partial t} + \nabla \cdot (\rho \vec{v}) = 0 \tag{1}$$

$$\rho\left(\frac{\partial \vec{v}}{\partial t} + \vec{v} \cdot \nabla \vec{v}\right) = -\nabla P + \nabla[\mu(\nabla \vec{v} + \nabla \vec{v}^{T})] \tag{2}$$

$$\rho c\left(\frac{\partial T}{\partial t} + \nabla(\vec{v} T)\right) = \nabla \cdot (K \nabla T) + S_v \tag{3}$$

Table 1 – Chemical composition of AZ31 and ZK60 magnesium alloys (wt.%) [22].

	Zn	Al	Si	Mg	Zr	Mg
AZ31	**0.79**	**2.83**	0.026	0.35	–	Balance
ZK60	**5.23**	-	0.002	0.003	0.465	Balance

where ρ [kg/m^3], k [W/(m·K)], c [J/(kg·°C)] are the density, thermal conductivity and specific heat of material, respectively; μ is the temperature and strain rate dependent viscosity [Pa·s]; $\vec{v}$ is the velocity vector of the plastic material flow [m/s]; P represents the pressure [Pa]; T is the local temperature of the workpiece [K]; S_v is the energy source term [N/m^3].

To better understand the dissimilar materials mixing mechanism, different alloys are usually treated as different phases in the CFD model [24]. Thus, two metal phases, including AZ31 and ZK60 alloys were considered and the VOF technique was applied to predict the flow of the dissimilar pair. The equation of VOF is given as [27,28]:

$$\frac{\partial F}{\partial t} + \nabla \cdot (\vec{v} F) = 0 \tag{4}$$

where F means the phase volume fraction of the cell.

3.2. Material properties

The densities of the AZ31 and ZK60 magnesium alloys are taken as constant, and these were 1860 kg/m^3 [29] and 1865 kg/m^3 [30], respectively. The thermal conductivity and the specific heat are temperature dependent, which can be calculated as

- For the AZ31 alloy [29].

$$k_{AZ31} = -300.35 + 2.2711T - 4.3 \times 10^{-3}T^2 + 3 \times 10^{-6}T^3 \tag{5}$$

$$c_{AZ31} = -1722.1 + 16.1T - 3 \times 10^{-2}T^2 + 2 \times 10^{-5}T^3 \tag{6}$$

- For the ZK60 alloy [31].

$$k_{ZK60} = -379.8 + 3.384T - 7.219 \times 10^{-3}T^2 + 5.087 \times 10^{-6}T^3 \tag{7}$$

$$c_{ZK60} = -3971.0 + 35.52T - 8.071 \times 10^{-2}T^2 + 6.075 \times 10^{-5}T^3 \tag{8}$$

It is well known that solid materials can be considered as fluids with extremely high viscosity in CFD modeling of friction stir welding process [24]. In this work, solid metals are also considered as fluids with high viscosity. Since the materials are treated as non-Newtonian fluids, the viscosity is strain rate dependent and can be written following the work of Colegrove et al. [32]:

$$\mu = \frac{\sigma}{3\dot{\varepsilon}} \tag{9}$$

where $\dot{\varepsilon}$ is the strain rate [/s]; σ is the flow stress [MPa], which is determined by temperature and strain rate of the material and is given as [33,34]:

$$\sigma = \frac{1}{\alpha}\ln\left\{\left[\frac{\dot{\varepsilon}}{A}\exp\left(\frac{Q}{RT}\right)\right]^{\frac{1}{n}} + \left[\left[\frac{\dot{\varepsilon}}{A}\exp\left(\frac{Q}{RT}\right)\right]^{\frac{2}{n}} + 1\right]^{\frac{1}{2}}\right\} \tag{10}$$

where R is the gas constant; α [/MPa], A [/s], and n are material constants and Q [kJ/mol] is the activation energy for the plastic deformation, with these values detailed in Table 2.

Fig. 2 depicts that the viscosities of AZ31 and ZK60 alloys varies with temperature and strain rate. Prior to welding, namely when the temperature and strain rate are respectively around 300 K and 0/s, the materials possess extremely high viscosities, i.e., higher than 1.5×10^8 Pa·s. In addition, as the temperature and strain rate increase, the viscosities obviously decrease (see Fig. 2).

3.3. *Geometric model and boundary conditions*

The boundary condition for heat exchange, including convection and radiation at the workpiece surfaces away from the shoulders of the tools, can be expressed by [37]:

$$-k\frac{\partial T}{\partial \vec{n}} = h_c(T - T_0) + \sigma_s e\left(T^4 - T_0^4\right) \tag{11}$$

Table 2 – Material constants for the AZ31 [35] and ZK60 [36] magnesium alloys.

Alloy	α (/MPa)	A (/s)	n	Q (kJ/mol)
AZ31	0.0113	9.8194×10^{11}	6.178	158.732
ZK60	0.0098	5.3083×10^{12}	6.666	158.919

where $\vec{n}$ is the vector normal to the surface [m]; h_c is the heat convection coefficient [W/(m^2·k)]; σ_s is Stefan–Boltzmann constant; and e is the radiation emissivity.

The slip rate (δ), which is introduced to define the contact state between the tool and workpiece, can be given [38]:

$$\delta = 1 - \exp\left(-\frac{wr}{\delta_0 w_0 r_s}\right) \tag{12}$$

where δ_0 is a constant taken as 0.4; w_0 [rad/s] is the tool rotational speed, while w is the typical value of w_0; r [m] is the distance of the local position from the tool axis; and r_s [m] represents the radius of the shoulder.

Currently, the model of the temperature-dependent friction factor was proposed to predict the temperature history during friction stir welding [39,40], however, it ignored the tool/workpiece interfacial slip, which does not match with what occurs during the welding process. In this study, the friction coefficient that considers the slip rate is given accordng to the work of Shi et al. [41]:

$$\mu_f = 0.5\exp(-\lambda\delta wr) \tag{13}$$

The heat flux during the FSSW process is mainly generated due to the friction and plastic deformation at the contact interfaces between the tool and workpiece. The heat generation at the upper/bottom surfaces of the shoulder and pins in contact with the workpiece can be calculated [42]:

$$q_s = \frac{J_w}{J_w + J_T}\left[(1-\delta)\eta\tau + \delta\mu_f P_N\right]wr \tag{14}$$

$$\tau = \frac{\tau_y}{\sqrt{3}} \tag{15}$$

$$J = \sqrt{k\rho c} \tag{16}$$

where J_w and J_T separately represent the thermal emissivity of the workpiece and tool, which can be calculated by Eq. (16); η is the mechanical efficiency; P_N is the plunge pressure, which takes 30 MPa here; τ_y is the yield stress [MPa], which is temperature dependent as Table 3 shows.

Furthermore, the heat generation at the sides of the pins is given as [42].

$$q_{ps} = \frac{J_w}{J_w + J_T}\left[(1-\delta)\eta\tau + \delta\mu_f\tau_y\right]wr \tag{17}$$

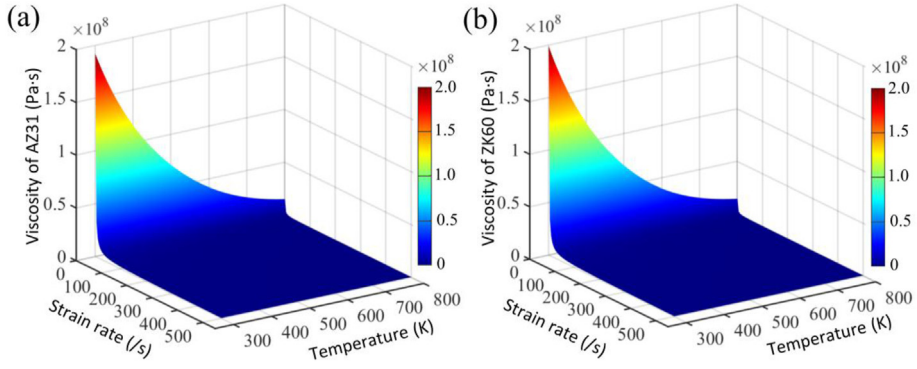

Fig. 2 – Viscosity variation with temperature and strain rate for: (a) AZ31 magnesium alloy, (b) ZK60 magnesium alloy.

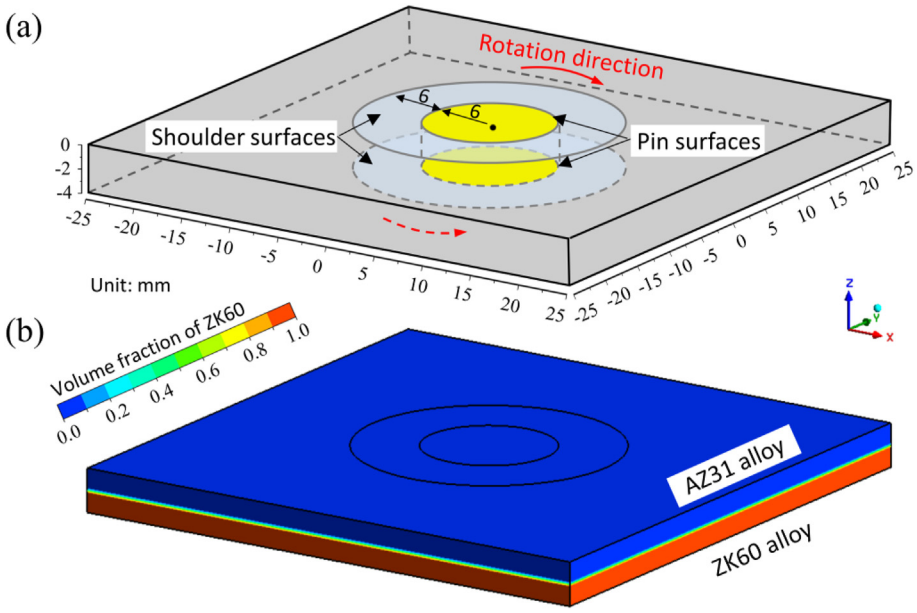

Fig. 3 – Calculation domains: (a) Geometric model; (b) Initial phase distribution.

3.4. *Numerical solution method*

As shown in Fig. 3, a calculated domain with dimensions of 50 mm × 50 mm × 4 mm was used and the thicknesses of the AZ31 and ZK60 plates are 2 mm. Prior to the simulation, the initial temperature and velocity are separately set as 300 K and 0 m/s according to the actual conditions experienced by the materials to be processed. The governing equations and equations for the heat flux and material flow are thermo-mechanically coupled and solved to calculate the multi-physics by using the SIMPLE algorithm. The numerical simulation is conducted in a transient procedure with an adaptive time step varied from 1×10^{-3} to 1×10^{-8} s. For better convergence during the simulation of the plunging and rising stages, the time step is further limited to less than 1×10^{-6} s. In addition, the dynamic mesh method [45], is used to imitate the movement of the pins during the plunging and rising stages.

4. Model validation

As Fig. 4 depicts, the experimental results [22], including the cross-section image and element distribution, were chosen to validate the numerical model for the Flat DSAT FSSW process. The calculated thermo-mechanically affected zone (TMAZ) is always represented by the region where the velocity of plastic material is non-zero [46,47]. Thus, the iso-viscosity value of 4×10^6 Pa·s, above which no significant plastic material flow occurs (Fig. 5a), can be treated as the predicted TMAZ boundary. Fig. 5a show that the measured and predicted TMAZ boundaries correspond well, suggesting that the proposed model is reliable in simulating the welding process. Since the two substrates have obvious compositional differences as shown in Table 1, electron probe microanalysis (EPMA) analysis of the Zn and Al elemental distribution was performed to further study the material mixing and weld interface characteristics of the joint as depicted in Fig. 4b and c. It can be seen that at the welded interface between the upper and lower pin/shoulder sides, there is an obvious dilution of Zn and Al, suggesting that elemental mixing occurs. Moreover, elemental exchange is also observed. In particular, Al, which is only present in the AZ31 plate (refer to Table 1), is transported to the ZK60 side during welding. Fig. 5b and 5c shows the calculated Zn and Al element distribution on the cross-section after welding. The elemental mixing and exchange phenomena are presented with a good correspondence with the experimental results detailed in Fig. 4b and c. These results suggest that due to the use of the adjustable pins, the two plates are strongly mixed around the joint interface through a strong material flow.

Table 3 – Temperature-dependent yield stress of the AZ31 [43] and ZK60 [44] magnesium alloys.

Yield stress (MPa)	Temperature (K)				
	300	373	473	523	573
AZ31	190	137	/	57	/
ZK60	118	/	77	43	22

5. Results and discussion

5.1. *Transient temperature field*

Fig. 6 depicts the simulated transient temperature field of the Flat DSAT FSSW process in the longitudinal cross-section. The temperature on the cross-section (y = 0 mm), extracted from the centrosymmetric computational domain, is used to demonstrate the thermal evolution. During the pre-heating stage (0–2 s), the temperature in the region near the upper

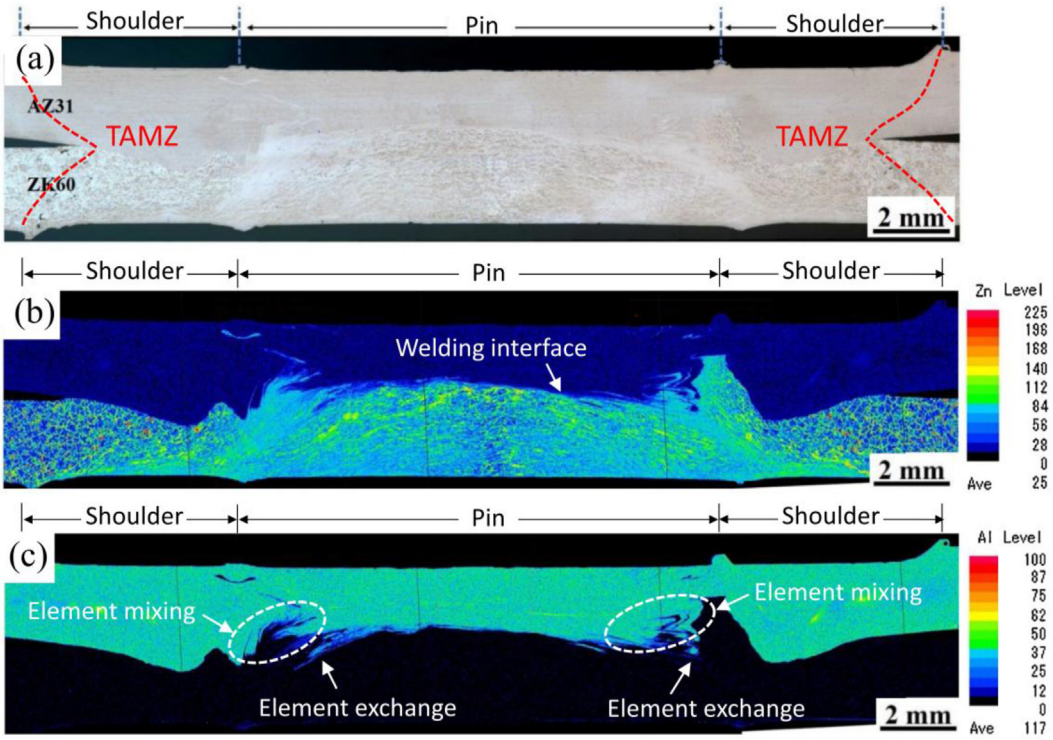

Fig. 4 – Experimental results: (a) cross-section image, (b) and (c) Zn and Al element distribution determined via EPMA measurements (reproduced from ref. [22], with permission from Elsevier).

and lower sided shoulders increases and a peak value of 540 K at 2 s is obtained. After, the upper sided pin plunges downward and a keyhole with a depth of 2.5 mm forms at $2 + \Delta t$ s as detailed in Fig. 6c, in which Δt is the plunging time as previously mentioned. Owing to the previous pre-heating process, the temperature increased and the materials softened, a bulge region occurs after the plunging stage in the Flat DSAT FSSW process as observed by Wang et al. [22]. During the welding stage ($2+\Delta t$-$4+\Delta t$ s), the temperature keeps rising and it reaches to its highest (670 K) at $4 + \Delta t$ s, which is 76.31% of the material melting point, 878 K [29]. After $2\Delta t$ s, which corresponds to the rising time, the lower sided pin rises upward and the keyhole is fully eliminated as Fig. 6e shows. During $4+3\Delta t$-$6+3\Delta t$ s (post-heating stage), the whole region between the pins and partial regions near the shoulders are heated to the maximum temperature, suggesting that the plates are well joined.

Fig. 7 further demonstrates the 3D view of the temperature field in the pre-heating stage (2 s) and welding stage ($4 + \Delta t$ s). It can be found that the peak temperature occurs on the pin-workpiece interface during the pre-heating stage, while it changes to the bulge region during the welding stage. Fig. 8 is the schematic diagram of Fig. 7 on the cross-section ($y = 0$ mm), in which the regions reach the peak temperatures, which are respectively 540 K and 670 K at the pre-heating stage and the welding stage. The regions away from the tools, which experience relatively lower temperature than the regions between the tools, are defined as low temperature regions, and the remaining regions are the high temperature regions. For this purpose, isotherms of 469 K and 561 K, which are separately the temperatures of the shoulder edges in Fig. 7a and b, are treated as the boundaries between the low and high temperature regions. In Fig. 8, the heat transfer through conduction, convection and radiation between the pre-heating and the welding stages are compared. The heat generates due to the friction and plastic deformation at the tool/workpiece interfaces and is then conducted perpendicular to the interfaces. Since the heat generation is higher than the radiant emission as Eq. 14–17 suggest, the high and peak temperature regions are always between the upper and lower tools. As Fig. 7a and Fig. 8a show, the peak temperature (540 K) occurs on the pin-workpiece interface at 2 s, which is away from the pin center and avoids the lower temperature region. During the welding stage, as depicted in Fig. 7a and Fig. 8a, the heat conduction conditions in the bulge region during the welding stage becomes more complex compared to the pre-heating stage, namely the location is heated by the lower pin surface and shoulder side and away from the pin center and lower temperature region, resulting in a peak temperature there.

5.2. *Material flow field*

Fig. 9 shows the calculated velocity field of the plastic material flow velocity at the longitudinal cross-section in the Flat DSAT FSSW process. During the pre-heating stage, the plastic material rotates around the pins and shoulder as depicted in Fig. 9b. The peak velocity of material flow is about 16.10 mm/s, which occurs near the edge of the shoulders. Because of the small rotation speed of the pin center, there is less material

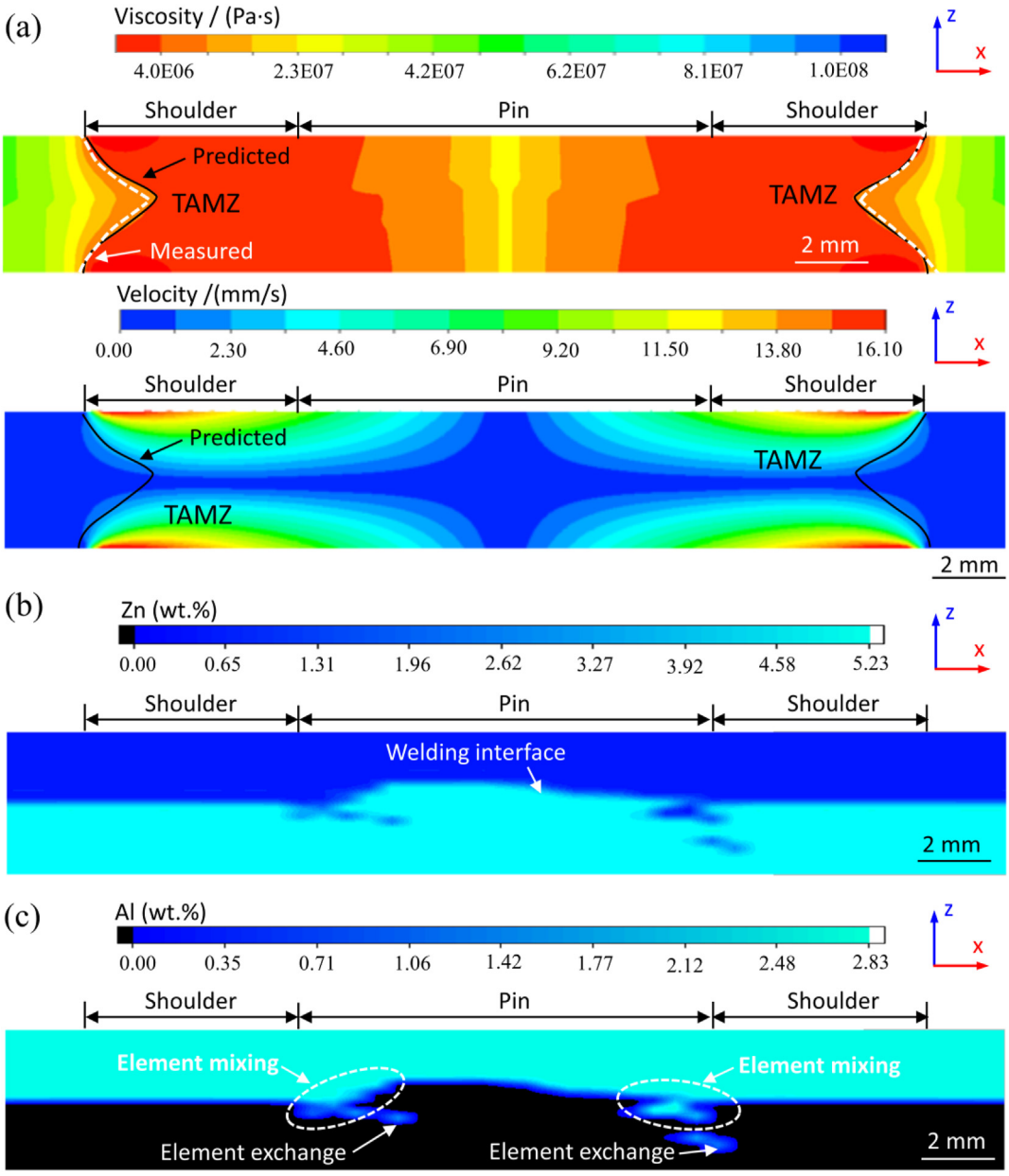

Fig. 5 – Calculated results on the cross-section (y = 0 mm) at the end of Flat DSAT FSSW process (6+3Δt s): (a) viscosity and velocity, (b) and (c) Zn and Al distribution. (Δt is the plunging time.)

flow in the area between the upper and lower pin centers. In the plunging stage, affected by the downward movement of the pins, the region between the pins experiences a vertical velocity of 1500 mm/s, which equals to the plunging speed. During the plunging process, the side of the upper pin contacts the workpiece that generates sufficient heat and leads to softening the material. Thus, the upper pin rotates and drives the material near the pin side to move, resulting in a larger flow area near the upper tool as shown in Fig. 9c. In the welding stage, the pins stop the vertical movement and the peak velocity of the material returns to 16.10 mm/s, occurring near the shoulder edges. The contour of the velocity field near the upper tool is similar to that of the conventional single-sided friction stir welding case [42], while it changes near the lower tool due to the position deviation of upper and lower pins. As Fig. 9d depicts, driven by the side of the lower shoulder, a relatively lager region of the plastic material flow near the lower pin appears compared to the region near the upper pin. During the rising stage, similar to the plunging stage, the rising region between the pins moves upward with a speed of 1500 mm/s. In the post-heating process, as shown in Fig. 9f, since the keyhole is fully eliminated, the material flow behavior is nearly the same as that in the pre-heating stage (refer to Fig. 9b).

Fig. 10 depicts the evolution of the welding interface of the AZ31 and ZK60 plates during the Flat DSAT FSSW process. As shown in Fig. 10a and b, there is no significant change of the welding interface during the pre-heating process since there is

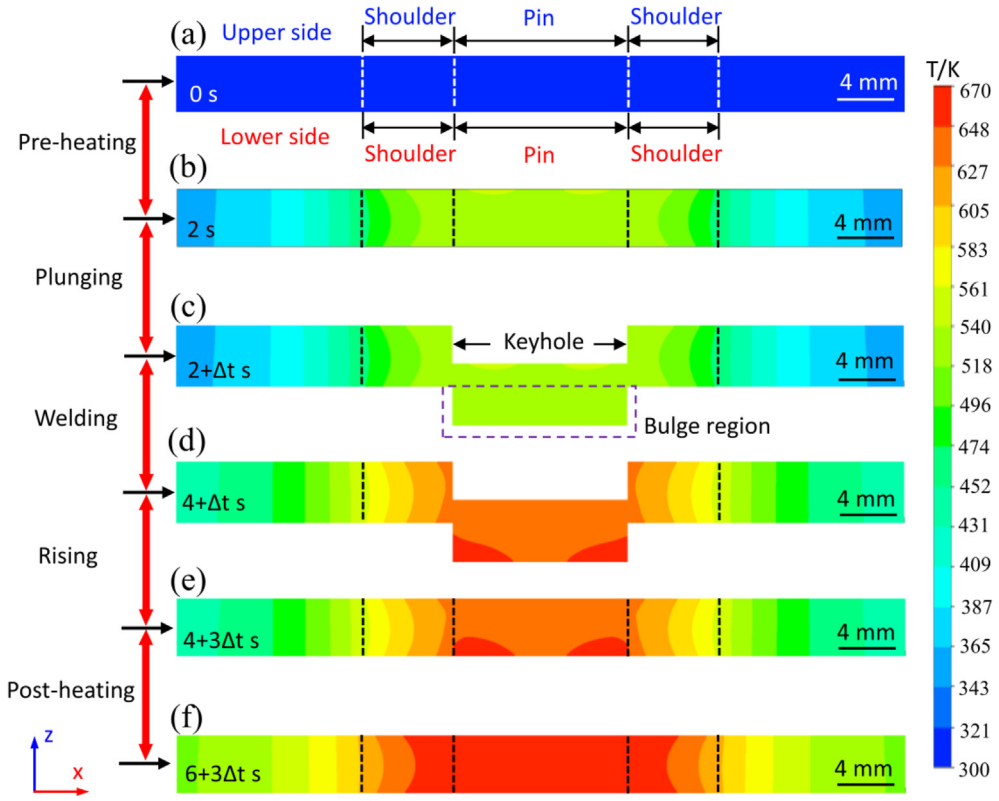

Fig. 6 – Temperature field on the cross-section (y = 0 mm) during Flat DSAT FSSW process.

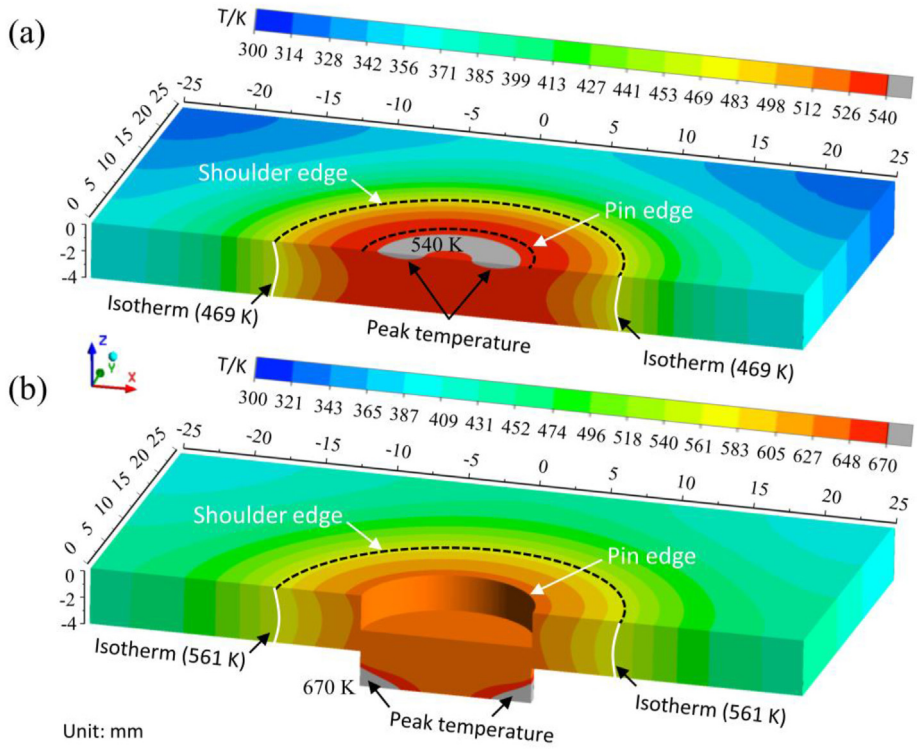

Fig. 7 – 3D view of the temperature field at: (a) pre-heating stage (2 s), (b) welding stage (4 + Δt s).

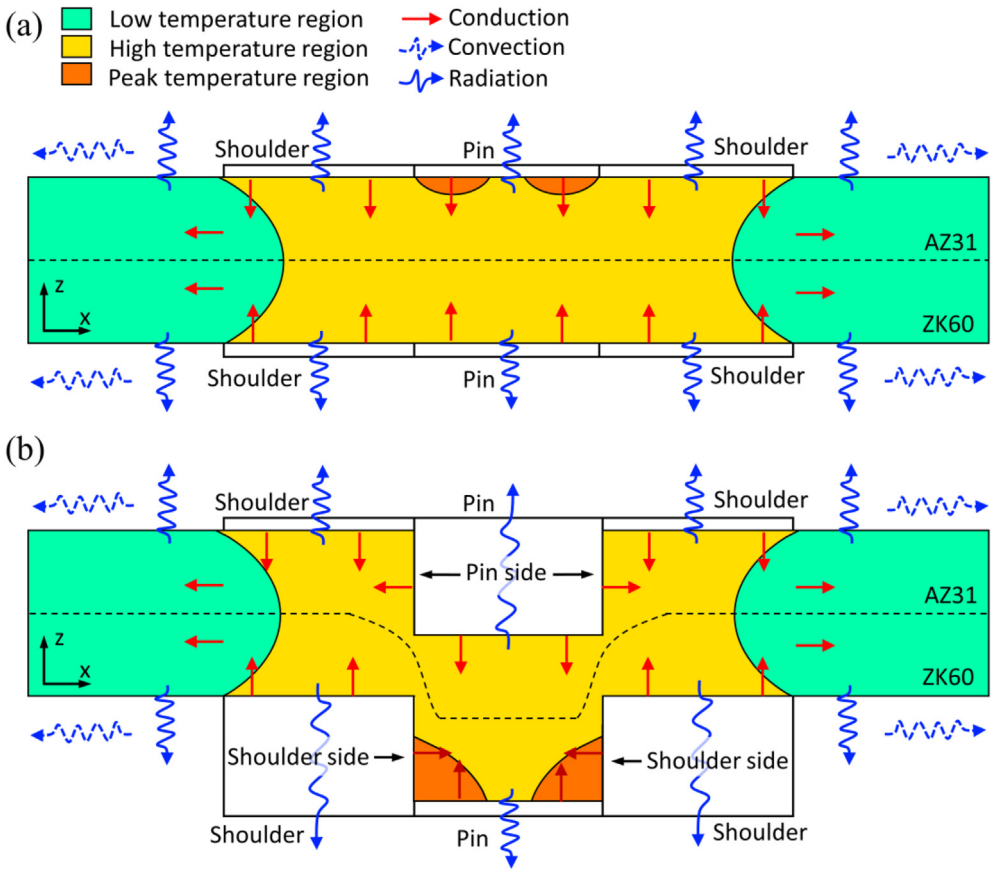

Fig. 8 – Diagram of the heat transfer conditions on the cross-section (y = 0 mm) in the Flat DSAT FSSW process during: (a) pre-heating stage, (b) welding stage.

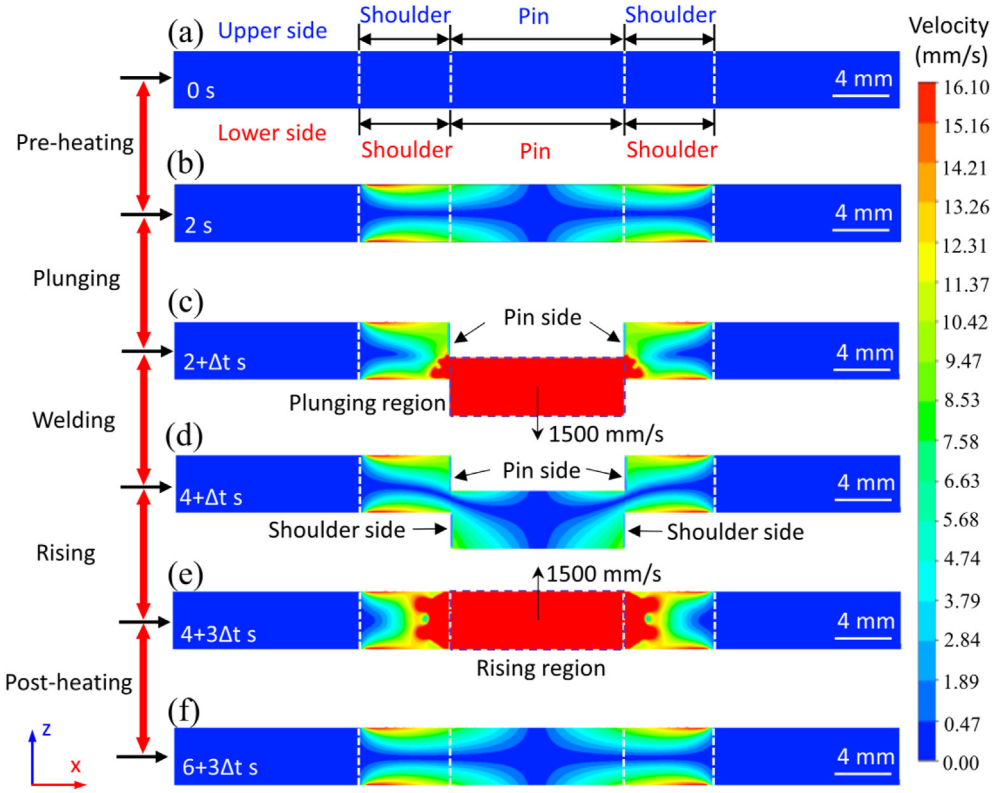

Fig. 9 – Plastic material flow velocity on the cross-section (y = 0 mm) during Flat DSAT FSSW process.

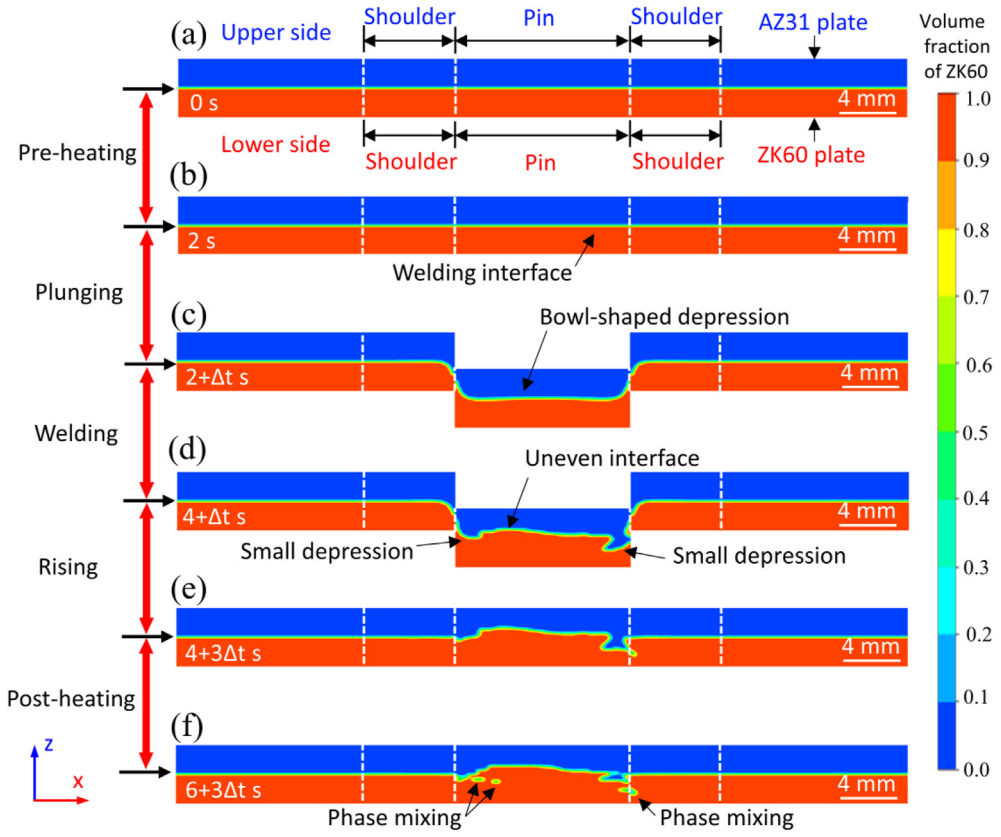

Fig. 10 – Evolution of the welding interface on the cross-section (y = 0 mm) during Flat DSAT FSSW process.

little plastic material flow near the interface as Fig. 10b suggests. As detailed in Fig. 10c, due to the plunging of the pins, a bowl-shaped depression occurs at the interface between the upper and lower pins that corresponds well to the results of Wang et al. [18,22]. During the welding stage, as mentioned previously, the regions near the lower pin and the side of the lower shoulder experience relatively extensive plastic material flow, resulting in an uneven interface and small depressions, as detailed in Fig. 10d. After the rising of the pins (Fig. 10e), the bowl-shaped depression at the interface is eliminated. During the post-heating process, the interface between the pins slightly fluctuates and phase mixing phenomenon occurs due to the rotation of the pins and shoulders.

Fig. 11 depicts the calculated 3D view of the material flow and distribution at the welding stage (4 + Δt s). The plastic material flow mainly occurs between the upper and lower tools, and the flow tendency on the tool/workpiece interface is consistent with the rotation direction of the nearby tool. Fig. 12 shows the material flow direction and phase distribution at different horizontal slices of the region between the tools. Analyzing Fig. 12a and b, which respectively correspond to the sections at half the thickness of AZ31 plate (z = −1 mm)

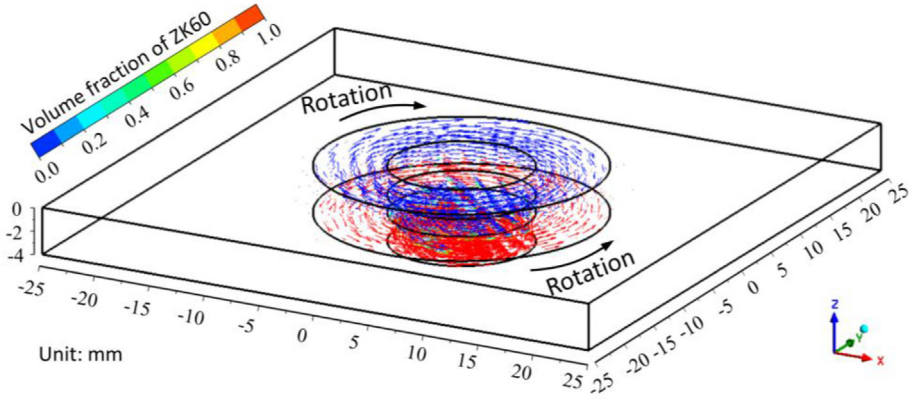

Fig. 11 – 3D view of the calculated material mixing and distribution in the model at the welding stage (4 + Δt s). (The small arrows presents the material flow direction, while the color of those arrows detail the local volume fraction of ZK60 phase.).

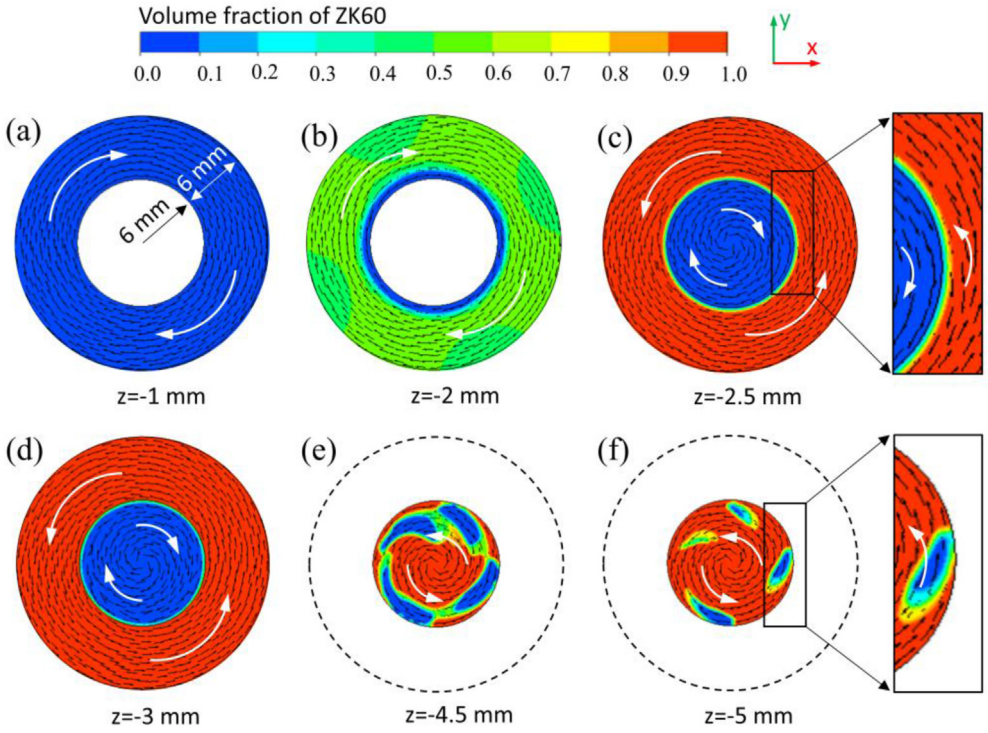

Fig. 12 – 3D view of the calculated material mixing and distribution on different horizontal sections at the welding stage (4 + Δt s). (The small black arrow presents the local material flow direction, while the white curved arrow means the flow tendency.)

and the initial boundary of AZ31/ZK60 plates (z = −2 mm), the plastic material flows clockwise which is the same as the rotation direction of the upper tool. On the upper pin/workpiece interface (z = −2.5 mm, Fig. 12c) and the section of half the thickness of AZ31 plate (z = −3 mm, Fig. 12d), the plastic material away from the upper pin flows counterclockwise consistent with the rotation direction of the lower tool, while the material near the upper pin flows clockwise driven by the upper tool. On sections z = −4.5 mm (Fig. 12e) and z = −5 mm (Fig. 12f) in the bulge region, the plastic material has a tendency to flow counterclockwise and phase mixing occurs owning to the extensive plastic material flow as Fig. 9d suggests.

6. Conclusions

A coupled thermo-hydrodynamic transient model is developed to understand the thermal process, plastic material flow behavior and welding interface evolution during Flat DSAT FSSW of AZ31 and ZK60 magnesium alloys. The model is considered to be reliable and was validated by experimentally-obtained data. The major conclusions are summarized as follows:

1) Owing to the previous pre-heating process, the material between the tools is softened. After the plunging process, a keyhole forms below the upper pin while a bulge region forms in the bottom of the plates. Subsequently, the lower-sided pin rises upward and the keyhole is fully eliminated.
2) During the welding stage, the heat conduction conditions in the bulge region becomes more complex compared with that of the pre-heating stage, resulting in a peak temperature there.
3) Due to the plunging of the pins, the welding interface between the upper and lower pins is bowl-shaped. During the welding stage, it grows uneven because of the extensive plastic material flow. After the post-heating process, the interface slightly fluctuates and phase mixing phenomenon occurs driven by the rotated tools.
4) By using the adjustable double-sided pins, after welding the whole region between the tools are heated to a maximum temperature of 670 K. In addition, the two plates are strongly mixed around the welding interface through a strong material flow, suggesting that the plates are well joined.

Declaration of Competing Interest

The authors declare that they have no known competing financial interests or personal relationships that could have appeared to influence the work reported in this paper.

Acknowledgements

This work was supported by Natural Science Foundation of China (No. 51775091, 52175292), Science and Technology Project of Sichuan Province (No. 2020ZDZX0015). JPO

acknowledges Fundação para a Ciência e Tecnologia (FCT) for its financial support through the project UIDB/00667/2020 (UNIDEMI). The authors also thank Xiaopei Wang and his group at Osaka University for their efforts in the related experimental research.

Appendix A. Supplementary data

Supplementary data to this article can be found online at https://doi.org/10.1016/j.jmrt.2022.01.097.

REFERENCES

[1] Joost WJ, Krajewski PE. Towards magnesium alloys for high-volume automotive applications. Scripta Mater 2017;128:107–12. https://doi.org/10.1016/j.scriptamat.2016.07.035.
[2] Singh VP, Patel SK, Ranjan A, Kuriachen B. Recent research progress in solid state friction-stir welding of aluminium–magnesium alloys: a critical review. J Mater Res Technol 2020;9:6217–56. https://doi.org/10.1016/j.jmrt.2020.01.008.
[3] Hirsch J, Al-Samman T. Superior light metals by texture engineering: optimized aluminum and magnesium alloys for automotive applications. Acta Mater 2013;61:818–43. https://doi.org/10.1016/j.actamat.2012.10.044.
[4] Bruni C, Forcellese A, Gabrielli F, Simoncini M. Effect of temperature, strain rate and fibre orientation on the plastic flow behaviour and formability of AZ31 magnesium alloy. J Mater Process Technol 2010;210:1354–63. https://doi.org/10.1016/j.jmatprotec.2010.03.025.
[5] Cao X, Jahazi M, Immarigeon J, Wallace W. A review of laser welding techniques for magnesium alloys. J Mater Process Technol 2006;171:188–204. https://doi.org/10.1016/j.jmatprotec.2005.06.068.
[6] Chiuzuli FR, Batistão BF, Bergmann LA, Alcântara NG, Santos Benjamin JF, Klusemann B, et al. Effect of the gap width in AZ31 magnesium alloy joints obtained by friction stir welding. J Mater Res Technol 2021;15:5297–306. https://doi.org/10.1016/j.jmrt.2021.10.115.
[7] Yin YH, Sun N, North TH, Hu SS. Hook formation and mechanical properties in AZ31 friction stir spot welds. J Mater Process Technol 2010;210:2062–70. https://doi.org/10.1016/j.jmatprotec.2010.07.029.
[8] Sun YF, Fujii H, Sato Y, Morisada Y. Friction stir spot welding of SPCC low carbon steel plates at extremely low welding temperature. J Mater Sci Technol 2019;35:733–41. https://doi.org/10.1016/j.jmst.2018.11.011.
[9] Yuan W, Mishra RS, Carlson B, Verma R, Mishra RK. Material flow and microstructural evolution during friction stir spot welding of AZ31 magnesium alloy. Mater Sci Eng 2012;543:200–9. https://doi.org/10.1016/j.msea.2012.02.075.
[10] Xu ZW, Li ZW, Ji SD, Zhang LG. Refill friction stir spot welding of 5083-O aluminum alloy. J Mater Sci Technol 2018;34:878–85. https://doi.org/10.1016/j.jmst.2017.02.011.
[11] Lyu XC, Li M, Li XF, Chen J. Double-sided friction stir spot welding of steel and aluminum alloy sheets. Int J Adv Manuf Technol 2018;96:2875–84. https://doi.org/10.1007/s00170-018-1710-x.
[12] Cox CD, Gibson BT, DeLapp DR, Strauss AM, Cook GE. A method for double-sided friction stir spot welding. J Manuf Process 2014;16:241–7. https://doi.org/10.1016/j.jmapro.2013.10.006.
[13] Wang XP, Morisada Y, Fujii H. Flat friction stir spot welding of low carbon steel by double side adjustable tools. J Mater Sci Technol 2021;66:1–9. https://doi.org/10.1016/j.jmst.2020.06.015.
[14] Wang X, Morisada Y, Fujii H. High-strength Fe/Al dissimilar joint with uniform nanometer-sized intermetallic compound layer and mechanical interlock formed by adjustable probes during double-sided friction stir spot welding. Mater Sci Eng 2021;809:141005. https://doi.org/10.1016/j.msea.2021.141005.
[15] Wang X, Morisada Y, Ushioda K, Fujii H. Double-sided friction stir spot welding of ultra-high strength C-Mn-Si martensitic steel by adjustable probes. J Mater Process Technol 2022;30:117422. https://doi.org/10.1016/j.jmatprotec.2021.117422.
[16] He XC. Thermo-mechanical modelling of friction stir welding process. Adv Mater Res 2013;774–776:1155–9. https://doi.org/10.4028/www.scientific.net/AMR.774-776.1155.
[17] Shi L, Wu CS, Liu HJ. The effect of the welding parameters and tool size on the thermal process and tool torque in reverse dual-rotation friction stir welding. Int J Mach Tool Manufact 2015;91:1–11. https://doi.org/10.1016/j.ijmachtools.2015.01.004.
[18] Wang XP, Morisada Y, Fujii H. Flat friction stir spot welding of AZ31B magnesium alloy using double side adjustable tools: microstructure and mechanical properties. Sci Technol Weld Join 2020;25:644–52. https://doi.org/10.1080/13621718.2020.1802896.
[19] Mandal S, Rice J, Elmustafa AA. Experimental and numerical investigation of the plunge stage in friction stir welding. J Mater Process Technol 2008;203:411–9. https://doi.org/10.1016/j.jmatprotec.2007.10.067.
[20] Garcia-Castillo FA, Reyes LA, Garza C, Lopez-Botello OE, Hernandez-Munoz GM, Zambrano-Robledo P. Investigation of microstructure, mechanical properties, and numerical modeling of Ti6Al4V joints produced by friction stir spot welding. J Mater Eng Perform 2020;29:4105–16. https://doi.org/10.1007/s11665-020-04900-z.
[21] Xiong JT, Peng X, Shi JM, Wang Y, Sun JR, Liu XZ, et al. Numerical simulation of thermal cycle and void closing during friction stir spot welding of AA-2524 at different rotational speeds. Mater Char 2021;174:110984. https://doi.org/10.1016/j.matchar.2021.110984.
[22] Wang XP, Morisada Y, Fujii H. Interface strengthening in dissimilar double-sided friction stir spot welding of AZ31/ZK60 magnesium alloys by adjustable probes. J Mater Sci Technol 2021;85:158–68. https://doi.org/10.1016/j.jmst.2021.01.024.
[23] Yang C, Wu CS, Shi L. Modeling the dissimilar material flow and mixing in friction stir welding of aluminum to magnesium alloys. J Alloys Compd 2020;843:156021. https://doi.org/10.1016/j.jallcom.2020.156021.
[24] Hasan AF. CFD modelling of friction stir welding (FSW) process of AZ31 magnesium alloy using volume of fluid method. J Mater Res Technol 2019;8:1819–27. https://doi.org/10.1016/j.jmrt.2018.11.016.
[25] Liu X, Chen G, Ni J, Feng Z. Computational fluid dynamics modeling on steady-state friction stir welding of aluminum alloy 6061 to TRIP steel. J Manuf Sci Eng 2017;139:051004. https://doi.org/10.1115/1.4034895.
[26] Sun Z, Wu CS. A numerical model of pin thread effect on material flow and heat generation in shear layer during friction stir welding. J Manuf Process 2018;36:10–21. https://doi.org/10.1016/j.jmapro.2018.09.021.
[27] Raeini AQ, Blunt MJ, Bijeljic B. Modelling two-phase flow in porous media at the pore scale using the volume-of-fluid method. J Comput Phys 2012;231:5653–68. https://doi.org/10.1016/j.jcp.2012.04.011.

[28] Ke WC, Oliveira JP, Cong BQ, Ao SS, Qi ZW, Peng B, et al. Multi-layer deposition mechanism in ultra high-frequency pulsed wire arc additive manufacturing (WAAM) of NiTi shape memory alloys. Additive Manufacturing 2022;50:102513. https://doi.org/10.1016/j.addma.2021.102513.
[29] Singh AK, Sahlot P, Paliwal M, Arora A. Heat transfer modeling of dissimilar FSW of Al 6061/AZ31 using experimentally measured thermo-physical properties. Int J Adv Manuf Technol 2019;105:771–83. https://doi.org/10.1007/s00170-019-04276-y.
[30] Du X, Du WB, Wang ZH, Liu K, Li SB. Simultaneously improved mechanical and thermal properties of Mg-Zn-Zr alloy reinforced by ultra-low content of graphene nanoplatelets. Appl Surf Sci 2021;536:147791. https://doi.org/10.1016/j.apsusc.2020.147791.
[31] Ma H, Wang J, Wang H, Dong N, Zhang J, Jin P, et al. Influence of nano-diamond content on the microstructure, mechanical and thermal properties of the ZK60 composites. J Magnes Alloy 2021. https://doi.org/10.1016/j.jma.2021.03.034.
[32] Colegrove PA, Shercliff HR. 3-Dimensional CFD modelling of flow round a threaded friction stir welding tool profile. J Mater Process Technol 2005;169:320–7. https://doi.org/10.1016/j.jmatprotec.2005.03.015.
[33] Sheppard T, Jackson A. Constitutive equations for use in prediction of flow stress during extrusion of aluminium alloys. Mater Sci Technol 1997;13:203–9. https://doi.org/10.1179/mst.1997.13.3.203.
[34] Yang C, Wu CS, Gao S. Modified constitutive equation by using phase field simulation of dynamic recrystallization in friction stir welding. J Mater Res Technol 2021;12:916–29. https://doi.org/10.1016/j.jmrt.2021.03.031.
[35] Liu J, Cui ZS, Li CX. Modelling of flow stress characterizing dynamic recrystallization for magnesium alloy AZ31B. Comput Mater Sci 2008;41:375–82. https://doi.org/10.1016/j.commatsci.2007.04.024.
[36] He YB, Pan QL, Liu X, Li B. Study of hot compression behavior of ZK60 magnesium alloy at elevated temperature. Adv Mater Res 2010;154–155:1–10. https://doi.org/10.4028/www.scientific.net/AMR.154-155.1.
[37] Ke WC, Bu XZ, Oliveira JP, Xu WG, Wang ZM, Zeng Z. Modeling and numerical study of keyhole-induced porosity formation in laser beam oscillating welding of 5A06 aluminum alloy. Opt Laser Technol 2021;133:106540. https://doi.org/10.1016/j.optlastec.2020.106540.
[38] Nandan R, Ro GG, Lienert TJ, Debroy T. Three-dimensional heat and material flow during friction stir welding of mild steel. Acta Mater 2007;55:883–95. https://doi.org/10.1016/j.actamat.2006.09.009.
[39] Sun Z, Wu CS. Influence of tool thread pitch on material flow and thermal process in friction stir welding. J Mater Process Technol 2020;275:116281. https://doi.org/10.1016/j.jmatprotec.2019.116281.
[40] Mohan R, Jayadeep UB, Manu R. CFD modelling of ultra-high rotational speed micro friction stir welding. J Manuf Process 2021;64:1377–86. https://doi.org/10.1016/j.jmapro.2021.02.060.
[41] Shi L, Wu CS, Padhy GK, Gao S. Numerical simulation of ultrasonic field and its acoustoplastic influence on friction stir welding. Mater Des 2016;104:102–15. https://doi.org/10.1016/j.matdes.2016.05.001.
[42] Shi L, Wu CS. Transient model of heat transfer and material flow at different stages of friction stir welding process. J Manuf Process 2017;25:323–39. https://doi.org/10.1016/j.jmapro.2016.11.008.
[43] Quan GF. Yield and plastic deformation of Mg-alloy AZ31 at elevated temperatures. Adv Mater Res 2005;488–489:623–8. https://doi.org/10.4028/www.scientific.net/MSF.488-489.623.
[44] Wu W, Hong CM, Chen LJ, Wang Y, Yang L, Li F, et al. High-temperature mechanical properties of as-extruded ZK60. Adv Mater Res 2005;488–489:753–7. https://doi.org/10.4028/www.scientific.net/MSF.488-489.753.
[45] Yu ZZ, Zhang W, Choo H, Feng ZL. Transient heat and material flow modeling of friction stir processing of magnesium alloy using threaded tool. Metall Mater Trans A 2012;43:724–37. https://doi.org/10.1007/s11661-011-0862-1.
[46] Sing AK, Sahlot P, Paliwal M, Arora A. Heat transfer modeling of dissimilar fsw of al 6061/az31 using experimentally measured thermo-physical properties. Int J Adv Manuf Technol 2019;105(2):771–83. https://doi.org/10.1007/s00170-019-04276-y.
[47] Nandan R, Roy GG, Debroy T. Numerical simulation of three-dimensional heat transfer and plastic flow during friction stir welding. Metall Mater Trans A 2006;37(4):1247–59. https://doi.org/10.1007/s11661-006-1076-9.